Journal of Materials Research and Technology 33 (2024) 9580–9594

Contents lists available at ScienceDirect

Journal of Materials Research and Technology

journal homepage: www.elsevier.com/locate/jmrt

Depth-dependent energy absorption control of large pulsed electron beam (LPEB) irradiations for defect-free surface modification of metallic alloys

Yonghoon Lee [a,1], Yunjae Hwang [b,1], Hyung Wook Park [b], Yunsung Kang [c,d], Jisoo Kim [a,c,d,*]

[a] School of Advanced Science and Technology Convergence, Kyungpook National University (KNU), 2559, Gyeongsang-daero, Sangju-si, Gyeongbuk, 37224, Republic of Korea
[b] Department of Mechanical Engineering, Ulsan National Institute of Science and Technology, 50 UNIST-gil, Ulsan 44919, Republic of Korea
[c] Department of Precision Mechanical Engineering, Kyungpook National University (KNU), 2559 Gyeongsang-Daero, Sangju, Gyeongbuk, 37224, Republic of Korea
[d] Convergence Research Center of Mechanical and Chemical Engineering (CRCMCE), Kyungpook National University (KNU), 2559 Gyeongsang-daero, Sangju, Gyeongbuk, 37224, Republic of Korea

ARTICLE INFO

Handling editor: L Murr

Keywords:
Large pulsed electron beam (LPEB)
Energy beam
Surface finishing
Defect-free
Surface manufacturing
Depth-dependent energy absorption control

ABSTRACT

Electron beam surface finishing offers the ability to treat various materials and shapes while enhancing surface properties such as wear and corrosion resistance. However, its industrial application is limited by the formation of crater-like defects' pulse count, irradiation angle, and energy density, were optimized to achieve defect-free surfaces. By systematically investigating the synergistic effects of previously studied parameters (irradiation angle and energy density), the optimal conditions were established through strategic combination of these parameters, demonstrating enhanced surface quality and reduced defect formation. These were compared to previously optimized conditions that focused solely on increasing pulse counts. The new conditions significantly reduced the density of crater-like defects and produced smoother surfaces. This improvement is attributed to concentrated energy absorption near the surface and the creation of a high-temperature gradient, which prevents the introduction of non-metallic inclusions. Unlike conventional methods, where accumulated heat leads to phase transformations and reduces hardness and corrosion resistance, the new approach maintains a rapid cooling rate. This allows the surface to retain a fully martensitic phase even at 45 pulses, resulting in higher surface hardness. These findings highlight that the newly developed conditions not only produce defect-free surfaces but also impart enhanced mechanical properties. This approach suggests that future improvements in surface quality for electron beam-based processes can be achieved by considering adjustments to the irradiation angle and energy density.

1. Introduction

In recent years, there has been growing interest in fine structures within high-value-added industries such as semiconductors and medical fields. This has led to extensive research addressing issues like wear, friction, and corrosion that occur on these surfaces [1–3]. As structures become increasingly fine, these issues become more critical, resulting in a heightened demand for effective surface finishing techniques [4–7]. Mechanical polishing, one of the most common surface finishing methods, is capable of creating mirror-like surfaces [7]. However, it is time-consuming, costly, difficult to apply to fine structures, and often relies on inefficient manual labor [8,9]. Furthermore, it only enhances surface morphology without improving mechanical and chemical properties. Consequently, energy beam-based surface finishing processes have gained attention as a more efficient alternative [6].

Energy beam-based surface finishing involves irradiating the surface with high-energy beams to modify its morphology and surface properties. The most prominent techniques include laser and electron beam methods. Lasers utilize photons as an energy source to generate narrow and highly focused beams, though their effectiveness can be constrained by the material's absorptivity and surface complexity [10]. In contrast, electron beams use electrons as an energy source, allowing them to deliver energy deep into the material (electron transmission) [11]. This makes electron beams less affected by the material's absorptivity or

---

* Corresponding author. School of Advanced Science and Technology Convergence, Kyungpook National University (KNU), 2559, Gyeongsang-daero, Sangju-si, Gyeongbuk, 37224, Republic of Korea.
E-mail address: js.kim@knu.ac.kr (J. Kim).

[1] These authors contributed equally to this work.

https://doi.org/10.1016/j.jmrt.2024.11.254
Received 22 October 2024; Received in revised form 25 November 2024; Accepted 26 November 2024

surface complexity, leading to their recent prominence in the surface treatment industry [12,13].

The electron beam surface treatment technology was first pioneered by Proskurovsky et al. who developed the low energy high current electron beam (LEHCB) technique [14,15]. This technology was later also referred to as high current pulsed electron beam (HCPEB) or large pulsed electron beam (LPEB), all sharing the same fundamental operating principles for pulsed electron beam with differences mainly in terminology [16–18]. This groundbreaking research demonstrated the capability of electron beam surface modification to significantly enhance material properties through rapid melting and solidification processes. The Large Pulsed Electron Beam (LPEB) technique, specifically, irradiates a wide beam diameter of 60 mm with pulsed beams. This process rapidly melts and evaporates the surface, followed by cooling at a gradient of 10^7 K/s to induce a surface quenching effect [9,11,19,20]. This significantly improves surface quality and enhances properties such as hardness, wear resistance, and chemical stability [19–23]. However, the formation of crater-like defects on the surface after LPEB treatment poses the most significant obstacle to its practical application [24–29]. These defects critically impact product performance and lifespan, particularly in precision mold and semiconductor industries where extremely low error tolerances are required. The presence of these craters leads to increased friction, accelerated fatigue failure, and enhanced corrosion susceptibility, limiting the broader industrial application of LPEB technology and hindering technological innovation in high-value-added industries.

The formation of crater-like defects in LPEB-treated surfaces is attributed to several complex mechanisms, which vary depending on the material composition. In metallic alloys, two primary mechanisms contribute to defect formation: the evaporation of non-metallic inclusions with low boiling points (such as manganese sulfide in steel) and localized evaporation around materials with high thermal diffusivity (exemplified by carbon-rich regions in alloys) [19,30]. Even pure materials can create defects through crater formation caused by localized melting and explosion at the melt layer's bottom due to electron transmission, and through quenching stress [20]. Considering the mechanisms described above, it becomes apparent that a complex analysis of the interactions between electrons and the material is necessary.

Previous studies have attempted to address these issues primarily by increasing the pulse count of LPEB treatments, aiming to evaporate all non-metallic inclusions within the melt layer [23,31,32]. However, this approach shows limitations by focusing solely on the removal of non-metallic inclusions, only temporarily mitigating the issue without providing a fundamental solution to the aforementioned mechanisms. It also leads to the incorporation of new inclusions from the substrate, impeding significant reduction in overall defect density. This method has been criticized for insufficient examination of changes in previously reported excellent surface properties and for its limited effectiveness in comprehensively addressing various defect formation mechanisms. These limitations underscore the need for a more comprehensive approach that addresses the various defect formation mechanisms while maintaining the advantages of LPEB treatment.

This study aims to develop optimized LPEB irradiation conditions based on a new perspective of depth-dependent energy absorption, in order to maintain surface quality while overcoming surface defects. The relationship between LPEB irradiation conditions and surface properties (such as surface morphology and hardness) are investigated in terms of the depth-dependent absorption. A numerical analysis on the energy absorption, which varies with irradiation angle and energy density, is performed to derive the optimal energy beam conditions. Based on these findings, modified LPEB irradiation conditions are proposed that overcome the structural limitations of previous conditions, allowing for precise control of the interaction between electrons and the material to achieve optimal energy beam conditions.

The newly proposed conditions are systematically tested to evaluate their impact on surface performance. Quantitative assessments of crater defect density, surface roughness and surface hardness conducted using optical microscopy (OM), white light interferometry (WLI), and Vickers hardness tests. Additionally, the underlying mechanisms behind surface changes are comprehensively analyzed through a depth-dependent absorption model, metallurgical phase analysis, and X-ray diffraction (XRD). This multi-faceted approach ensures a thorough understanding of how the proposed irradiation conditions influence surface properties, contributing to the potential optimization of electron beam processes for defect-free surface treatments in various industries.

2. Experimental setup

2.1. Materials and equipment

As minimizing surface defects is crucial in the mold industry, American Iron and Steel Institute (AISI) H13 steel, a material widely used in mold manufacturing, was selected for the experiment. The chemical composition of AISI H13 steel is summarized in Table 1. The chemical composition of AISI H13 steel typically contains 5.1% chromium, 1.25% molybdenum, and 1.0% vanadium as its main alloying elements, with a carbon content of approximately 0.35%. This balanced composition is carefully designed to achieve optimal hot working performance. The chromium content provides good oxidation resistance and hardenability, while molybdenum enhances high-temperature strength and temper resistance. Vanadium forms fine carbides that contribute to wear resistance and help maintain grain size control [33,34]. The moderate carbon content ensures sufficient hardness while maintaining adequate toughness. These elements work synergistically to provide the steel with its characteristic properties suitable for hot work applications such as die casting dies, extrusion dies, and forging dies. Specimens were precisely machined to dimensions of 20 × 10 × 10 mm (width × length × height). The specimens were ground with SiC sandpaper (#1200) to ensure consistency in the results during the surface treatment.

The LPEB equipment was utilized for the surface treatment of AISI H13 substrates. The irradiation employs a particulate energy beam, wherein electrons impact the substrate surface, converting their kinetic energy into thermal energy. This energy conversion induces surface melting and evaporation, ultimately leading to surface modification. A schematic of the experimental setup is presented in Fig. 1a). As depicted, the LPEB apparatus comprises a vacuum chamber for mounting the substrate and an electron gun section responsible for generating and irradiating the electron beam. Initially, the specimen was placed within the vacuum chamber, and nitrogen gas was introduced to purge any remaining air. Following this, a high vacuum was established using a rotary pump in conjunction with a turbo molecular pump. Once the desired vacuum level was achieved, argon gas, acting as a plasma medium, was introduced to maintain the chamber pressure at 0.05 Pa. Upon stabilization of the chamber conditions, the specimen was exposed to electron beam irradiation. The process proceeds as follows: Voltage is applied to the anode (5 keV) of the electron gun, generating a Penning effect that ionizes the argon gas into plasma, which accumulates densely near the anode. The electrons are then accelerated by the voltage applied to the cathode and solenoid directed towards the specimen in an unfocused beam. When the beam is irradiated onto the specimen, two components affect the material: the beam's energy density and the pulse irradiation time. The pulse duration is fixed at the equipment's default value of 2 μs, and for electron beams, the energy density is expressed in terms of electron kinetic energy, with the energy density being

Table 1
The chemical composition of as-received American Iron and Steel Institute (AISI) H13 steel substrates [wt.%].

C	Si	Mn	P	S	Cr	Mo	V	Fe
0.35	1.00	0.25	0.030	0.020	5.10	1.25	1.00	Bal.

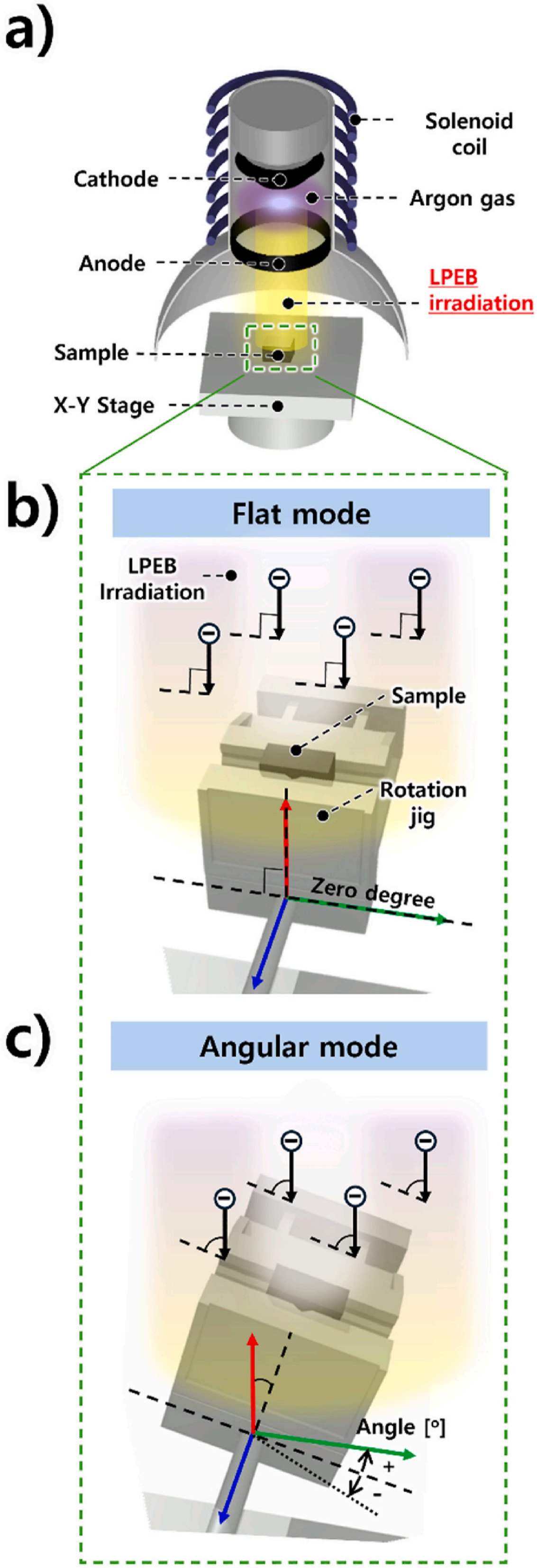

Fig. 1. Schematic diagram of the LPEB experimental setup. a) Consists of the LPEB equipment, b) Illustration of the Flat mode, where the substrate is irradiated at a zero-degree angle. c) Illustration of the Angular mode, where the substrate is irradiated at a specified angle (°).

represented by the manufacturer's empirical formula. The formula consists of factors including anode voltage, solenoid voltage, cathode voltage, irradiation distance, and Argon pressure, and these variables determine the energy density are listed on Table S1. The irradiation distance was fixed at 30 mm since longer distances reduce electron kinetic energy, and the anode voltage, which correlates with the total quantity of electrons, was maintained constant. The cathode voltage affects the electrons' linear directional kinetic energy, while the solenoid voltage influences their spiral direction.

The beam has a Gaussian profile with a 60 mm diameter, and the energy density variations according to this Gaussian profile are illustrated in Fig. S1. Given these characteristics and the sample size, it was assumed that the pulses were uniformly distributed across the material used in this study. The energy densities of 10 J/cm^2 and 5 J/cm^2 used in this research are capable of melting and even evaporating the surface to a depth of approximately under 10 μm, and it is known that higher energy density leads to deeper molten layers [35,36]. The specified energy density increases the surface temperature of the specimen to over 2,000°C within the short irradiation period of approximately 2 μs [17]. This intense thermal input is followed by rapid cooling, with heat dissipating through the specimen's bulk and the x-y stage, resulting in an extremely high cooling rate of approximately 10^7 K/s.

2.2. Variation of depth-dependent energy absorption

The absorption behavior along the depth direction is characterized by unique features specific to electron beams, which are distinct from energy density factors. Unlike laser processing where light energy is converted to thermal energy at the surface, electron beam processing involves the conversion of electron kinetic energy into thermal energy within the material. Notably, these moving electrons do not stop at the material surface but penetrate into the material. The interactions between electrons and materials, such as transmission and backscattering, result in a Gaussian distribution of thermal absorption along the depth direction, rather than the exponential decrease of thermal absorption profile at the surface seen in laser processing. Analysis of electron beam behavior has been developed based on Monte-Carlo simulation [11,37,38], and Cosslett et al. demonstrated that existing high-energy electron scattering theories were inadequate for low-energy electron regions, leading to their study of electron-material interactions in the 5–30 keV acceleration voltage range used in LPEB [39–41]. Subsequently, numerous studies have been conducted on the depth-dependent energy absorption of electrons in materials [11,20,26,41,42]. This theoretical framework for depth-dependent absorption has only been studied for electrons interacting with single materials. However, for composite or multilayer materials, the interactions between electrons and the different constituent materials may lead to different phenomena compared to single-material systems [36].

The electron beam characteristics vary depending on acceleration voltage, angle of incidence, and material properties, which are components of energy density. To derive factors related to depth-dependent energy absorption, a comprehensive analysis of electron-material interactions is essential. When considering the interactions between electrons and the material as a total of 100%, these interactions can be divided into three components: transmission, backscattering, and scattering. Transmission occurs when electrons pass through the material without colliding with atoms, gradually losing energy through interactions with the material's electrons until they eventually stop at a certain depth [39,42]. Backscattering, a significant source of energy loss in electron beams, happens when incident electrons collide with atoms in the material and are deflected back towards the surface, resulting in energy loss near the surface [11]. Scattering refers to electrons changing direction within the material due to collisions with atoms or electrons, during which the electron's kinetic energy is transferred to the material. The scattering process represents the absorption phenomenon that occurs as electrons lose their kinetic energy. This absorption of electron kinetic energy is essentially converted into thermal energy in the material, and the proportion of scattered electrons directly correlates to the material’s energy absorption rate. Understanding these interactions is crucial for accurately predicting and controlling energy penetration depth and distribution in processes such as LPEB treatment. The sum of these three components equals one, and based on this, the electron energy absorption n_A can be calculated. The degree of absorption n_A is defined as follows, using the backscattering rate n_B and the transmission rate n_T [39–41]:

$$n_A = 1 - n_B - n_T, \tag{1}$$

After the electron beam reaches the material, the transmission rate n_T represents the fraction of electrons that pass through the material. This rate is influenced by several variables, including the atomic number Z of the material, the angle of incidence θ, the depth z_{depth}, and the maximum penetration depth R. The transmission rate n_T is calculated using the following equation [43]:

$$n_T = \exp\left(- m_1(Z,\theta) \times \left(z_{\text{depth}}/R\right)^{m_2(Z,\theta)} \Big/ \left(1 - \left(z_{\text{depth}}/R\right)^{m_3(Z,\theta)}\right)\right), \tag{2}$$

The parameters m_1, m_2, and m_3 are functions of Z and θ, which modulate the transmission rate by adjusting the rate’s decrease with depth, the curvature of the transmission profile, and how the rate approaches zero as the depth reaches R.

The maximum penetration depth R is calculated as follows [42]:

$$R = \left(2.76 \times 10^{-2} \times M_a \times E_0^{5/3}\right) \Big/ Z^{8/9}$$
$$\times \cos(\theta)$$
$$\times \left(1 + 0.978 \times 10^{-3} \times E_0\right)^{5/3} \Big/ \left(\left(1 + 1.957 \times 10^{-3} \cdot E_0\right)^{4/3} \times \left(\rho \times 10^9\right)\right), \tag{3}$$

where M_a represents the atomic mass of the material, E_0 is the acceleration voltage, and ρ is the density of the material. This equation describes the depth within the material that electrons can penetrate before their energy is significantly diminished.

Fig. S2 illustrates the variation in transmission rate n_T as a function of different acceleration voltages and angles of incidence. The results indicate that higher acceleration voltages and smaller angles of incidence lead to increased transmission rates, which is critical for understanding the depth-dependent energy absorption.

In the context of electron beam interactions, the backscattering coefficient n_B is another important factor that influences the overall energy absorption by the material. The backscattering coefficient is calculated using the following equation [43,44]:

$$n_B = B^{1-\kappa(1-\cos(\theta))}, \tag{4}$$

where B is the backscattering factor, which is determined by the equation:

$$B = \beta \times \left(1 - \exp\left(- 0.0066 \times \beta^{-5/2} \times Z\right)\right), \tag{5}$$

The parameter β is calculated based on the acceleration voltage E_0 as follows:

$$\beta = 0.4 + 0.065 \times \log(E_0), \tag{6}$$

Additionally, κ is an energy-dependent weighting factor, defined by the equation:

$$\kappa = 1 - \exp\left(-1.83 \times E_0^{0.25}\right), \tag{7}$$

Fig. S3 illustrates how the backscattering coefficient change with varying acceleration voltage and angle of incidence. The backscattering coefficient data reveals that lower acceleration voltages and larger angles of incidence lead to an increase in the backscattering coefficient. This increase significantly impacts the energy loss due to backscattering, which plays a crucial role in calculating the depth-dependent energy absorption.

Using Equation (1), the depth-dependent absorption can be calculated, which is crucial for understanding the formation of surface defects such as craters. The degree of energy absorption represents the portion of electron energy absorbed by the material after accounting for energy lost to backscattering and transmission. Moreover, this model incorporates corrections based on interactions between different depth layers, allowing us to accurately determine the absorption as a function of depth.

The results demonstrate that this model effectively explains the tendency for maximum absorption to occur at specific depths within the material, which is closely related to the formation of surface defects. Fig. 2 illustrates the depth-dependent energy absorption for AISI H13 steel under various electron beam energies and angles of incidence. As reported in previous studies, the maximum energy absorption does not occur at the surface but rather at a certain depth within the material [11,

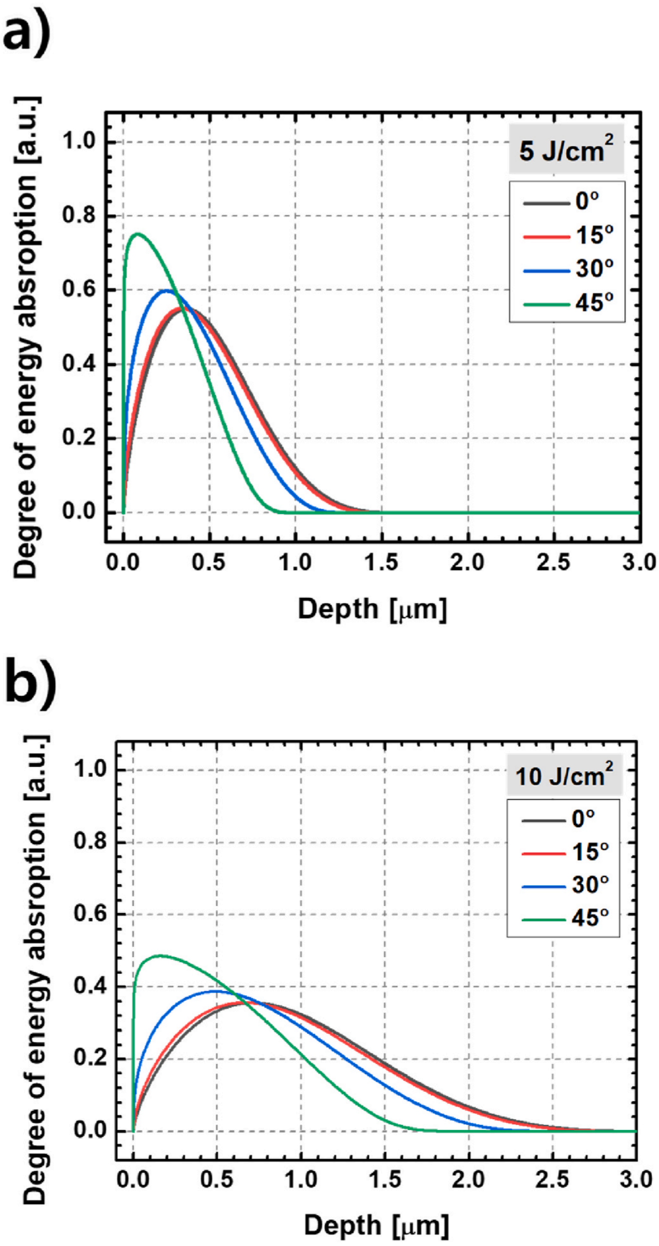

Fig. 2. Degree of absorption for AISI H13 steel at various electron beam energies and incidence angles with energy density of a) 10 J/cm^2 and b) 5 J/cm^2.

23]. Fig. 2a) and b) confirm this phenomenon, showing that when comparing electron beams with energies of 5 J/cm^2 and 10 J/cm^2, the depth of the maximum degree of absorption is shallower at the lower energy of 5 J/cm^2. This trend shows the observation that the depth of the maximum degree of absorption decreases as the angle of electron beam incidence increases and as the energy density decreases, which consequently affects the molten layer thickness. Representative cross-sectional images showing the molten layer thickness measurements under different angles and energy densities are presented in Fig. S4. These images strongly support Fig. 2, demonstrating that under the same energy density conditions, the molten layer thickness decreases as the angle increases and the energy density decreases.

2.3. *Experimental design*

The surface treatment of AISI H13 substrates was conducted utilizing LPEB equipment, which employs electrons as an energy source. Upon the electrons' impact on the substrate surface, their kinetic energy is converted into thermal energy, leading to the melting and evaporation of the surface, and subsequently altering its properties.

The conditions for LPEB irradiation are classified into two main modes: Flat Mode (FM) and Hybrid Angle Mode (HM). FM was designed to replicate findings from initial studies aimed at eliminating crater-like defects by adjusting the number of pulses while maintaining a fixed irradiation angle at 90°. For FM, the energy density was set at 10 J/cm^2, the irradiation angle at 0°, and the pulse numbers at 5, 10, 15, 20, 30, and 45. HM mode was developed by modifying the parameters related to degree of energy absorption in terms of depth from the LPEB conditions used in FM. This mode incorporates variations in both the irradiation angle (Fig. 1c)) and energy density and is further divided into HM with High Energy Finishing (HM-H) and Low Energy Finishing (HM-L). Specific details for FM, HM-H, and HM-L irradiation conditions are provided in Table 2. For HM, similar to FM 15, the first step proceeds with 15 pulses at 0° angle. Subsequently, step 2 irradiation is conducted by tilting at ± 30°. Particularly for HM-L, a lower energy density of 5 J/cm^2 was irradiated compared to FM and HM-H.

To form a uniform irradiated surface, the irradiation angle was adjusted to 30°. In Supporting data Fig. S5, insufficient irradiation was observed when tilted at 45°, and the hardness data in Fig. S5c) showed that the hardness in the area with insufficient irradiation was 40% lower than the highest hardness value. This occurred due to LPEB's characteristic of electron accumulation at the edges of the surface. To address this issue, a method of alternating between positive and negative irradiation at a 30° angle was chosen to prevent surface gradation and achieve uniform irradiation. This approach allowed for the formation of a defect-free surface and ensured uniform hardness throughout the material.

Understanding the interaction between electrons and the material is essential for identifying and optimizing the relationships between factors affecting degree of energy absorption in terms of depth. This requires precise calculations of backscattering, transmission, and penetration depth, all of which are influenced by factors such as the density of the substrate material, atomic mass, atomic number, energy density of the electron beam, and irradiation angle. These variables collectively determine the degree of energy absorption in terms of depth, enabling precise control over surface properties during the LPEB process.

2.4. *Material characterization*

The characterization of the LPEB-treated AISI H13 steel surface involved several analytical techniques to comprehensively assess surface morphology, defect structure, crystallography, and mechanical properties. Surface morphology and microstructural observations were conducted using an OM (Axiolab 5, Zeiss, Germany) with magnifications of 50× and 500×, respectively. After electron beam treatment, the surface was etched to reveal the microstructure, and multi-focus imaging techniques were employed. To obtain three-dimensional surface profiles and measure surface roughness, a WLI (NV-F2700, NanoSystem, Korea) was used. The collected data were processed with Nanomap software to correct surface slope and standardize the color scale.

Table 2
Electron beam irradiation conditions for Flat Mode (FM) and Hybrid Angle Mode (HM).

Flat mode (FM)	1st step		2nd step		Total irradiation pulse
	Energy density [J/cm^2]	Irradiation angle [°]	Energy density [J/cm^2]	Irradiation angle [°]	
Sample	10	0	–	–	
FM 5	5 pulses		–		5
FM 10	10 pulses		–		10
FM 15	15 pulses		–		15
FM 20	20 pulses		–		20
FM 30	30 pulses		–		30
FM 45	45 pulses		–		45
Hybrid angle mode with high energy finishing (HM-H)	**1st step (FM 15)**		**2nd step**		**Total irradiation pulse**
	Energy density [J/cm^2]	**Irradiation angle [°]**	**Energy density [J/cm^2]**	**Irradiation angle [°]**	
Sample	10	0	10	±30	
HM-H 20	15 pulses		5 pulses		20
HM-H 30	15 pulses		15 pulses		30
HM-H 45	15 pulses		30 pulses		45
Hybrid angle mode with low energy finishing (HM-L)	**1st step (FM 15)**		**2nd step**		**Total irradiation pulse**
	Energy density [J/cm^2]	**Irradiation angle [°]**	**Energy density [J/cm^2]**	**Irradiation angle [°]**	
Sample	10	0	5	±30	
HM-L 20	15 pulses		5 pulses		20
HM-L 30	15 pulses		15 pulses		30
HM-L 45	15 pulses		30 pulses		45

Additionally, XRD analysis was conducted using CuK-α radiation (SmartLab, Rigaku, Japan) to determine phase composition and crystallographic structure. The XRD measurements were carried out with a step size of 0.02° over a 2θ range from 40° to 100°. Surface hardness was evaluated using Vickers hardness tester (ZH μ m, Zwick Roell, Germany) to analyze changes in adhesive strength due to surface plastic deformation, specifically targeting the LPEB-resolidified layer, which is approximately 5 μm thick. The tests were performed using a Vickers diamond indenter with a minimum load of 0.01 kg to ensure that the hardness values accurately reflect the properties of the treated surface layer.

3. Results

3.1. *Surface morphology*

The surface morphology of LPEB-treated specimens was observed through OM (Fig. 3) and WLI (Fig. 4). While both instruments share the commonality of observing surface morphology through images, they differ in the format of these images. OM provides 2-dimensional images showing an optical top view and excels at capturing overall images at lower magnifications where focal differences are less pronounced. In contrast, WLI analyzes light diffraction patterns to produce 3-dimensional images through non-contact methods. This characteristic gives WLI an advantage at relatively higher magnifications and allows for

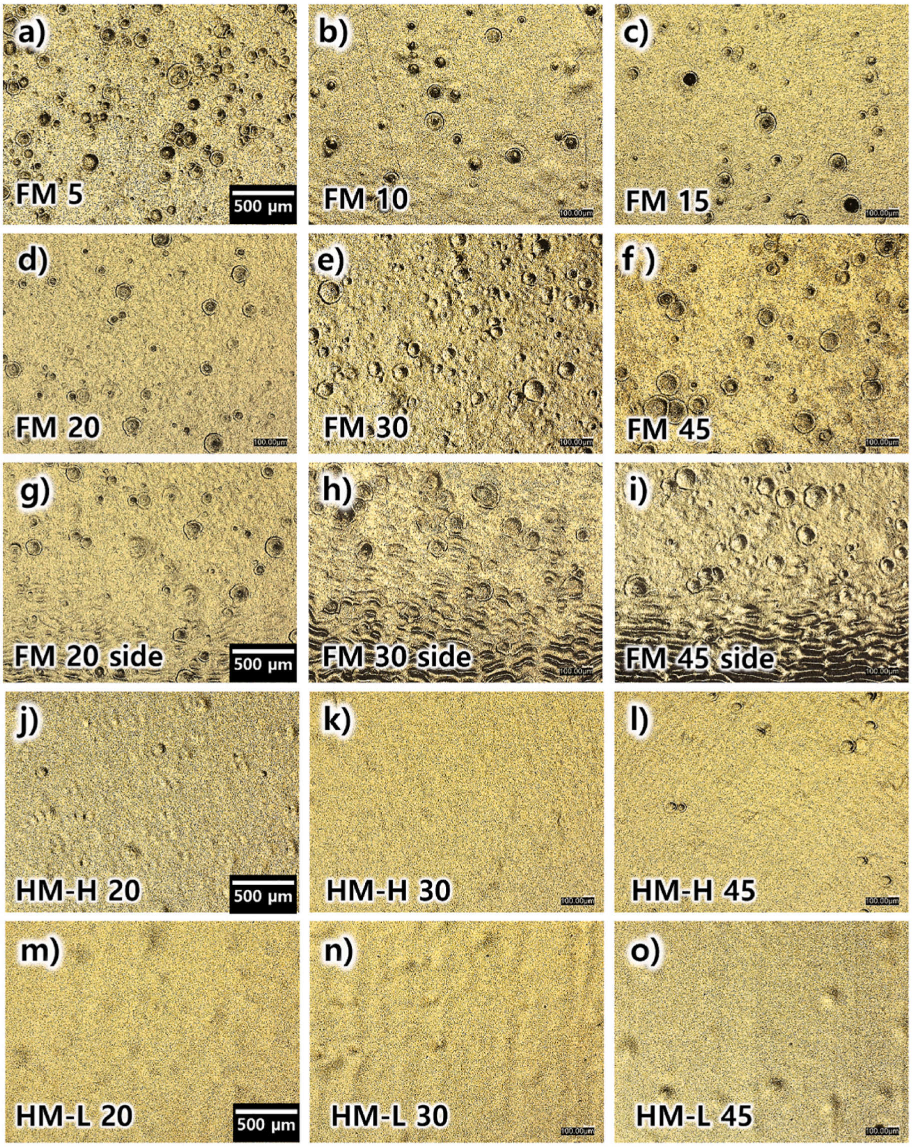

Fig. 3. Surface morphology and defect analysis of AISI H13 steel after LPEB treatment. Optical microscope (OM) images under Flat Mode (FM) conditions (FM 5 to FM 45; a) to f)), wave patterns at sample edges under FM conditions (g) to i)), and OM images under Hybrid Angle Mode with High Energy (HM-H 20 to HM-H 45; j) to l)) and Low Energy (HM-L 20 to HM-L 45; m) to o)).

undistorted visualization of surface topography with varying heights. Additional analysis is possible with WLI data, including the extraction of linear or areal surface roughness measurements. In this section, OM was used to observe the overall distribution of surface defects at low magnification, while WLI was employed to examine the approximate heights of distributed defects and evaluate the degree of surface smoothness. These qualitative data were used to quantify crater density and roughness data (Fig. 5).

Fig. 3a) to 3f) present OM images of samples treated under FM conditions from FM 5 to FM 45, showing that there is no clear trend in the reduction of defect distribution with increasing pulse counts, as numerous crater-like defects remain evident even at FM 45. Fig. 3g) to 3i) illustrate the wave patterns that emerged at the edges of the samples from FM 20 to FM 45, with these patterns becoming increasingly pronounced as the number of pulses increases. Conversely, Fig. 3j) to 3l) and Fig. 3m) to 3o) depict the results under HM-H and HM-L conditions, respectively. Under HM-H conditions, some crater-like defects are observed; however, they are significantly reduced compared to those under FM conditions. In contrast, under HM-L conditions, crater-like defects are scarcely observed.

Fig. 4 presents WLI images of samples treated under various LPEB conditions, providing three-dimensional views of the defects and allowing for precise height measurements. The color bar on the right indicates the height of the three-dimensional morphology. According to the WLI images, FM 5 exhibits crater-like defects with depths of approximately 8.5 μm. As the pulse count increases to FM 20, the defect depths decrease significantly to around 3.75 μm, representing a reduction of about 55.9%. This substantial decrease in defect depth demonstrates the initial effectiveness of increasing pulse counts in mitigating surface irregularities. However, the trend does not continue linearly with further increases in pulse count. Beyond FM 20, the defect depths begin to increase again, indicating a threshold effect in the LPEB treatment process. This observation suggests that there is an optimal pulse count for defect reduction, beyond which the treatment becomes less effective or potentially counterproductive. Interestingly, wave patterns are observed at the edges of the samples beginning from FM 20. These patterns show increased amplitude with higher pulse counts, reaching up to approximately 19 μm at FM 45 (Fig. 4g) to 4i)). This phenomenon suggests that increasing pulse counts beyond FM 20 leads to the formation of deeper craters and generates wave patterns at the sample

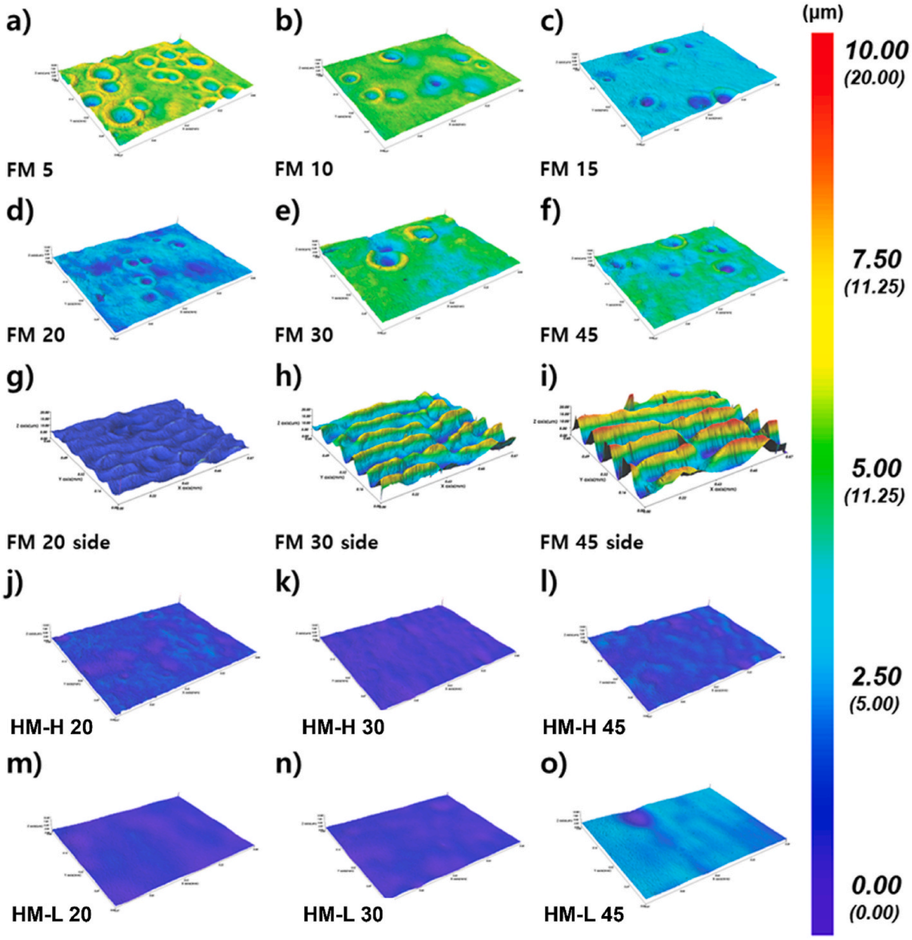

Fig. 4. Surface morphology and defect analysis of AISI H13 steel after LPEB treatment. Images captured using a white light interferometer under Flat Mode (FM) conditions (FM 5 to FM 45; a) to f)), wave patterns at the sample edges under FM conditions (g) to i)), and surface profiles under Hybrid Angle Mode with High Energy (HM-H 20 to HM-H 45; j) to l)) and Low Energy (HM-L 20 to HM-L 45; m) to o)). All images have a uniform size of 870 × 650 μm, and the maximum height scale is set to 10 μm for relative comparison, except for g) to i), where it is standardized to 20 μm. The color bar on the right indicates defect depths and surface height variations.

edges. In contrast, under HM-H and HM-L conditions, distinct crater shapes are not observed, and the surface height variations remain below 3 μm. This represents a further reduction of at least 20% compared to the lowest defect depth achieved with the FM conditions (3.75 μm at FM 20). The absence of distinct craters and the minimal surface height variations under these conditions demonstrate that the HM treatments consistently provide superior surface smoothness compared to the FM treatments.

The density of crater-like defects on AISI H13 steel samples after LPEB treatment was quantified based on surface morphology OM data, revealing distinct trends with varying pulse counts. Fig. 5a) presents the quantified results of a density of crater-like defects. At FM 5, the density of crater-like defects was highest, reaching $18 \times 10^7/\text{m}^2$. As the pulse count increased to FM 15, this density significantly decreased by 81.1% to $3.4 \times 10^7/\text{m}^2$. However, with further increases in pulse count, the density rose again, increasing by 73.5% from FM 15's $3.4 \times 10^7/\text{m}^2$ to stabilize around $5.9 \times 10^7/\text{m}^2$ at FM 45. Under HM-H and HM-L conditions, after initial irradiation at FM 15 (1st step in Table 2) levels, the density of crater-like defects did not increase with additional pulses but instead stabilized at $0.55 \times 10^7/\text{m}^2$ by a total pulse count of 30. At HM-H 45, there was a slight increase in defect density to approximately $2 \times 10^7/\text{m}^2$. Notably, the HM-L condition maintained under $1 \times 10^7/\text{m}^2$ defect density in all of the HM-L conditions. The surface roughness of AISI H13 steel samples after LPEB treatment was analyzed, showing clear variations with different pulse counts. Fig. 5b) shows the surface roughness (R_a) as a function of the total number of irradiation pulses for FM, HM-H, and HM-L conditions. Under FM conditions, the surface roughness starts at 0.55 μmR_a at FM 5, decreases to around 0.3 μmR_a at FM 15, and then increases significantly with further pulse counts, reaching up to 1.6 μmR_a at FM 45. Particularly, from FM 20 onwards, a high standard deviation is observed due to the formation of wave patterns on the surface, leading to instability in surface roughness values. In contrast, HM-H and HM-L conditions maintain relatively stable surface roughness across different pulse counts. The initial roughness values for HM-H and HM-L at a total pulse count of 20 are approximately 0.2 μmR_a and 0.3 μmR_a, respectively. As the pulse count increases, the low surface roughness is maintained, converging to ~0.2 μmR_a at a total pulse count of 30. Even at a total pulse count of 45, the surface roughness for HM-H and HM-L remains significantly lower than that of FM conditions.

3.2. *Mechanical properties and crystal structure*

Achieving reduced surface defect density is essential; however, a comprehensive surface treatment technology must maintain or enhance the inherent surface properties while improving surface smoothness. To validate this dual functionality, surface hardness measurements and XRD phase analysis were conducted. The surface hardness of AISI H13 steel samples following LPEB treatment was examined, revealing distinct trends across varying pulse counts. Fig. 6 depicts the Vickers surface hardness in relation to the total number of irradiation pulses for

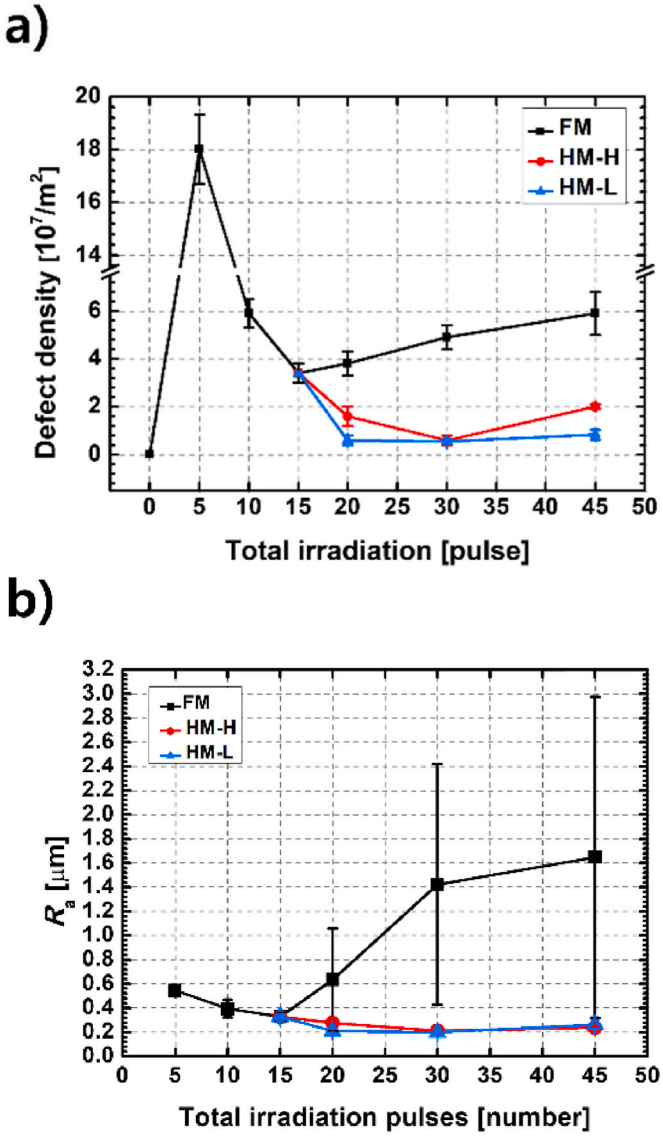

Fig. 5. Quantified data of AISI H13 steel samples after LPEB treatment under different modes (FM, HM-H, and HM-L) as a function of the total number of irradiation pulses: a) the density of crater-like defects, and b) surface roughness (R_a).

FM, HM-H, and HM-L conditions. The untreated bare surface showed a hardness value of 292 HV. Under FM conditions, surface hardness initially increases, rising from approximately 400 HV at FM 5 to around 840 HV at FM 15. However, it then gradually decreases with further pulse counts, dropping to around 449 HV at FM 45, representing a 46.5% reduction compared to FM 15. In contrast, HM-H conditions also show a decrease in surface hardness with increasing pulse count but maintain higher hardness levels compared to FM. The reduction in hardness reaches 652 HV at a total pulse count of 45, a decrease of 22.3% relative to FM 15. HM-L conditions exhibit the smallest reduction in surface hardness, with values remaining relatively stable across all pulse counts. The hardness reduction is within 4.0% of FM 15 across all pulse counts, with the hardness stabilizing at 806 HV by FM 45.

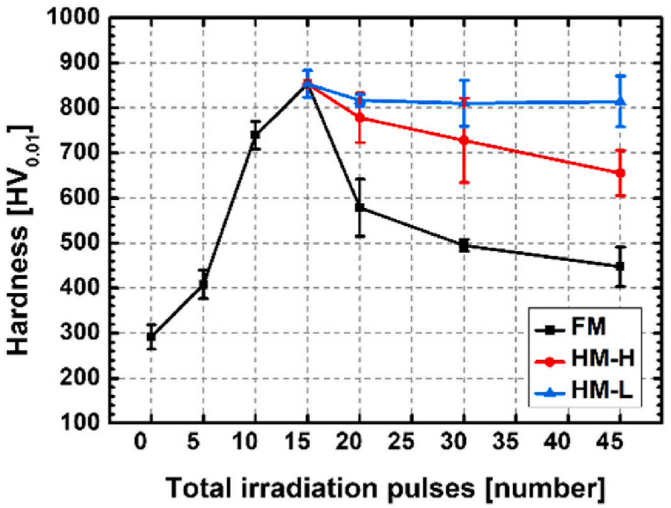

Fig. 6. Vickers surface hardness of AISI H13 steel samples after LPEB treatment as a function of the total number of irradiation pulses under different conditions (FM, HM-H, and HM-L).

Fig. 7a) to 7c) show normalized XRD patterns according to the electron beam pulse conditions in Table 2. Fig. 7a) presents the XRD patterns of AISI H13 steel treated under FM conditions. The untreated sample exhibited four peaks at 44.5°, 64.7°, 82.1°, and 98.7°, corresponding to ferrite peaks with (110), (200), (211), and (220) crystal planes, respectively. After electron beam irradiation, peak shifts were observed; notably, FM 5 showed the same ferrite peaks as the bare material, but the peak positions shifted to 44.8°, 65.9°, 82.6°, and 99.4°, representing shifts ranging from 0.5° to 1.2°. This rightward peak shift phenomenon was consistently observed in all LPEB-treated samples. In FM 10, the emergence of new peaks around 43°, 50°, 74°, and 90° is noteworthy, which were identified as austenite peaks with (111), (200), (220), and (311) crystal planes. These peaks formed in FM 10 persisted throughout all conditions with varying intensities. Martensite, having a Body-Centered Tetragonal (BCT) structure, exhibits peak broadening of ferrite peaks due to its structural similarity to the Body-Centered Cubic (BCC) structure of ferrite. Starting with subtle peak broadening near the (211) plane in FM 5, distinct broadening of ferrite peaks with (110), (200), and (211) planes became evident as conditions progressed from FM 5 to FM 10 and FM 15. Upon reaching FM 20, the broadened ferrite peaks began to sharpen again, a trend that continued up to FM 45, which had the maximum pulse count. Notably in FM 45, the austenite (111) peak grew to become a major peak alongside the ferrite (110) peak, which was previously the sole dominant peak. Fig. 7b) shows the XRD data under HM-H conditions. In the HM-H 20 sample, new austenite peaks emerged and martensite peaks exhibited a pattern similar to that observed in FM 10 and FM 15. From HM-H 30 onwards, similar to the phenomenon observed after FM 20, the ferrite peaks of (200) and (211) planes sharpened. Regarding the austenite peaks, while the austenite (111) peak was prominent in FM 45, the HM-H condition uniquely showed significant growth in both austenite (111) and (220) peaks, reaching their maximum intensities. At the maximum pulse count of HM-H 45, both the austenite (111) and (220) peaks emerged as the dominant peaks. Fig. 7c) shows the XRD data under HM-L conditions. Similar to FM 10 and FM 15, HM-L conditions exhibited newly formed austenite peaks and ferrite peak broadening due to martensite formation. Like HM-H conditions, growth of the austenite (220) peak was also observed. Notably, the ferrite (200) peak showed not only broadening but also peak splitting, and from HM-L 20 onwards, the austenite (200) peak showed significant growth, reaching its maximum intensity to become the dominant peak. The approximate phase volume fractions, quantified through XRD pattern fitting analysis, are illustrated in Fig. S6.

4. Discussions

4.1. Surface defect analysis

The most critical issue in LPEB treatment is the formation of crater-like defects. Through comprehensive analysis of qualitative and

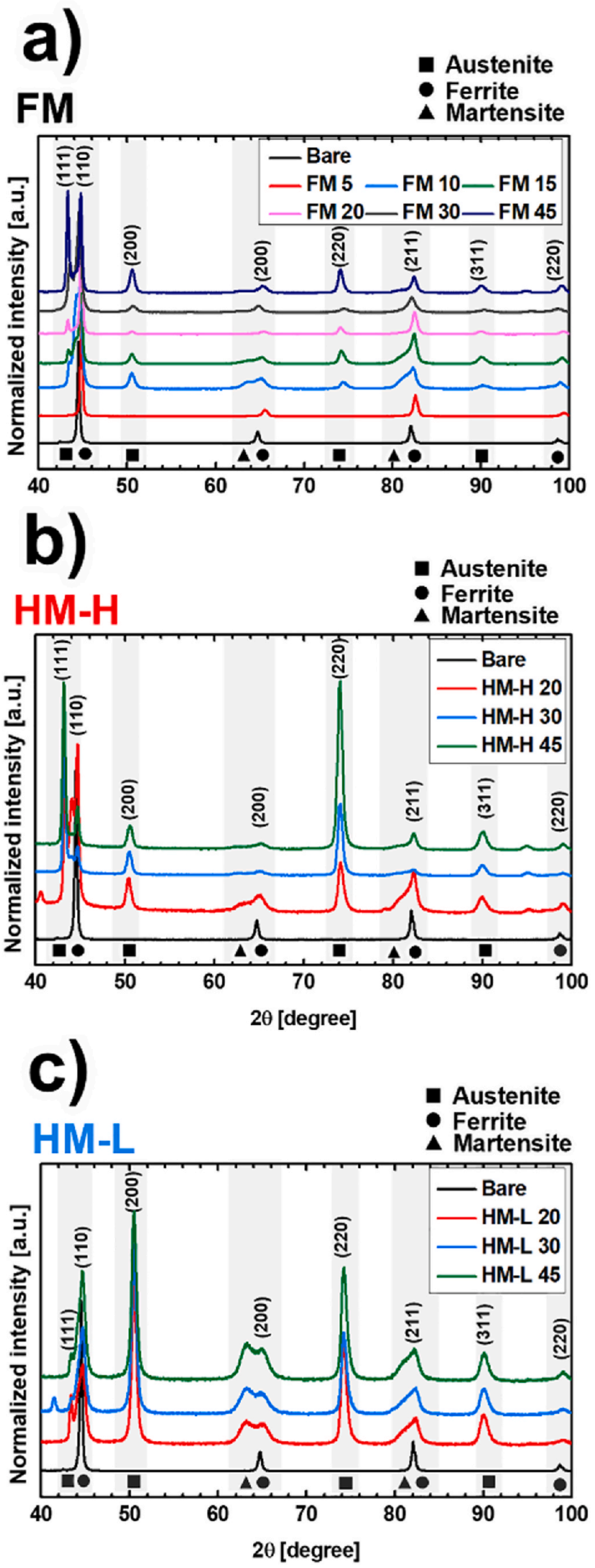

Fig. 7. X-ray diffraction (XRD) patterns for AISI H13 steel under different treatment modes: a) FM mode; b) HM-H mode; and c) HM-L mode.

quantitative results, the mechanism of crater formation can be inferred as follows: crater-like defects are primarily formed by vapor bubbles generated within the molten layer. During LPEB treatment, the surface temperature can locally exceed 2000 °C, causing the material to melt and partially evaporate [6]. After irradiation, the substrate undergoes rapid cooling with a gradient of approximately 10^7 K/s. This rapid cooling traps gas bubbles within the molten layer, which then burst and solidify, forming crater-like defects [25].

The formation of external gas in the molten layer that causes crater-like defects during LPEB treatment is primarily driven by two factors: the presence of non-metallic inclusions with different thermal properties and the temperature gradient within the molten layer caused by electron-material interactions. First, non-metallic inclusions (e.g., manganese sulfide; MnS) and materials with high thermal diffusivity (e.g., carbon) play crucial roles [25,29]. While non-metallic inclusions in energy beam industries typically include surface oxides and other products generated by energy beam interaction, in LPEB treatment, which occurs in a high-vacuum chamber, non-metallic inclusions refer to those existing internally in solid state. Non-metallic inclusions with lower evaporation points than steel evaporate within the molten layer, forming crater-like defects [28]. Conversely, materials like carbon, characterized by high evaporation points and thermal diffusivity, cause the surrounding substrate to evaporate, leading to similar defects [29]. These impurities and alloys with thermal properties different from the substrate significantly influence crater formation [25].

Second, the temperature gradient within the molten layer resulting from electron-material interactions plays a crucial role. Unlike laser treatment where the outermost surface reaches the highest temperature, LPEB uses electron kinetic energy, causing the maximum temperature to occur beneath the surface, as shown in Fig. 2 [11,20,26]. This subsurface heating can cause evaporation and explosion within the molten layer [25]. As heat penetrates deeper into the material, the maximum temperature shifts deeper, increasing the likelihood of crater formation. Due to electron transmission phenomena, localized melt pools with lower melting points from beneath the molten layer, which can burst upward through the molten layer due to quenching stress, forming craters [20, 26].

Previous studies aimed to eliminate non-metallic inclusions in the molten layer by repeatedly increasing the number of LPEB pulse treatments, as discussed in Table 2. While this method showed some effectiveness, it had significant limitations due to material-dependent variations and did not address all factors contributing to crater formation. This trend is shown in Fig. 5a). Under FM conditions, increasing the pulse count reduced defect density up to FM 15, however the reduction was not significant beyond this point. Even at FM 15, a crater-like defect density of $3.4 \times 10^7/\text{m}^2$ was observed. After FM 15, further increases in pulse count led to increases in crater-like defect density (Fig. 5a)), surface roughness (Fig. 5b)), crater depth (Fig. 4). This is attributed to increased molten layer depth and heat accumulation effects. Cross-sectional images showing the deepening molten layer thickness with increasing pulse count are presented in Fig. S4d) to S4i), clearly demonstrating the thickening of the molten layer with higher pulse counts. Previous research has shown that the increase in molten layer thickness is primarily caused by increased random distribution probability of abnormally high energy pulses and carbon accumulation in the extreme surface molten layer [35]. This increase in molten layer thickness, as shown in Fig. S4, serves to draw solid-state non-metallic inclusions from below into the molten layer, resulting in increased crater density and depth. While previous studies indicated that background temperature increase and heat accumulation had minimal effects on molten layer increase [35], heat accumulation can still influence crater formation in LPEB. The increase in material temperature enhances electron transmittance, consequently forming the maximum absorption depth lower down, as shown in Fig. 2. In this case, the number and scale of localized melt pools beneath the molten layer can increase dramatically. If these melt pools explode due to quenching stress, they can generate substantial additional craters. The shock waves from these explosions affect the liquid-state molten layer, creating crater-like defects and wave patterns. Fig. 8a) shows this mechanism. As the pulse count increases, both the number of localized melt pools beneath the molten layer and the intensity of shock waves increase, corresponding to the growing amplitude trend shown in Fig. 4g) to 4i). Therefore FM 15 with the lowest crater density and surface roughness sown to be the optimal condition in FM mode. Therefore, FM 15 was determined to be the optimal condition in FM mode, demonstrating the lowest crater density ($3.4 \times 10^7/m^2$) and surface roughness (1.6 μmR_a). However, these values still indicate significant surface defects, suggesting the limitations of the conventional FM approach.

Through this analysis, it was found that while initially increasing pulse count in FM mode effectively reduced defect density, this approach reached its limits due to increased molten layer depth and heat accumulation. To overcome these limitations, a new strategy was developed combining appropriate variations in incidence angle and energy density. This approach shows potential to compensate for the increased molten layer depth and heat accumulation associated with increased pulse counts. The experimental process began by replicating the conventional increasing pulse count conditions (FM 15) to establish a baseline. After determining the optimal point, additional comparisons were made by varying both incidence angle and energy density. This method enabled direct comparison between the conventional approach and new optimized conditions. Referring to Section 3, by combining conditions of increased incidence angle and decreased energy density, a hybrid condition can be designed to progressively reduce molten layer depth as pulse count increases. This strategy contributes to achieving high-quality surface characteristics by reducing absolute energy accumulation, preventing molten layer deepening, and preventing heat accumulation. Fig. 8b) illustrates the molten layer depth and crater formation mechanisms during the optimization process. The left portion shows crater deepening and intensified heat accumulation with increasing pulse count under FM conditions. The center and right portions demonstrate how HM-H and HM-L modes effectively maintain shallower molten layers by controlling electron beam incidence angle and energy density, significantly reducing crater formation and suppressing wave pattern occurrence. Experimental results show that at 45 pulses, the highest pulse count tested under HM conditions, crater density decreased by a minimum of 41.2% (HM-H) and a maximum of 70.6% (HM-L) compared to FM conditions, while surface roughness decreased by approximately 87% in all HM conditions. Notably, the HM-L 30 condition demonstrated optimal results with the lowest defect density ($0.55 \times 10^7/m^2$) and surface roughness (0.2 μmR_a). The HM-H mode applies high energy (10 J/cm^2) with increased incidence angles (0° to ±30°) for uniform surface irradiation, while the HM-L mode maintains the same incidence angles but uses lower energy (5 J/cm^2) to control depth-directional energy absorption more shallowly, focusing energy on the surface to reduce non-metallic inclusions within the molten layer. This is particularly significant considering that the non-metallic inclusions causing localized subsurface aggregation were minimally removed during the first step, FM 15.

Particularly noteworthy is that HM-L's absolutely lower energy accumulation and surface-concentrated energy distribution results in minimal heat accumulation, maintaining uniform and low crater density and surface roughness even with additional pulses. These results demonstrate that HM-H and HM-L modes successfully control molten layer depth, improve surface quality, and significantly reduce crater defects and wave pattern formation.

4.2. Metallurgical analysis

LPEB treatment is significant not only for its ability to smooth the surface layer through melting but also for imparting crucial surface

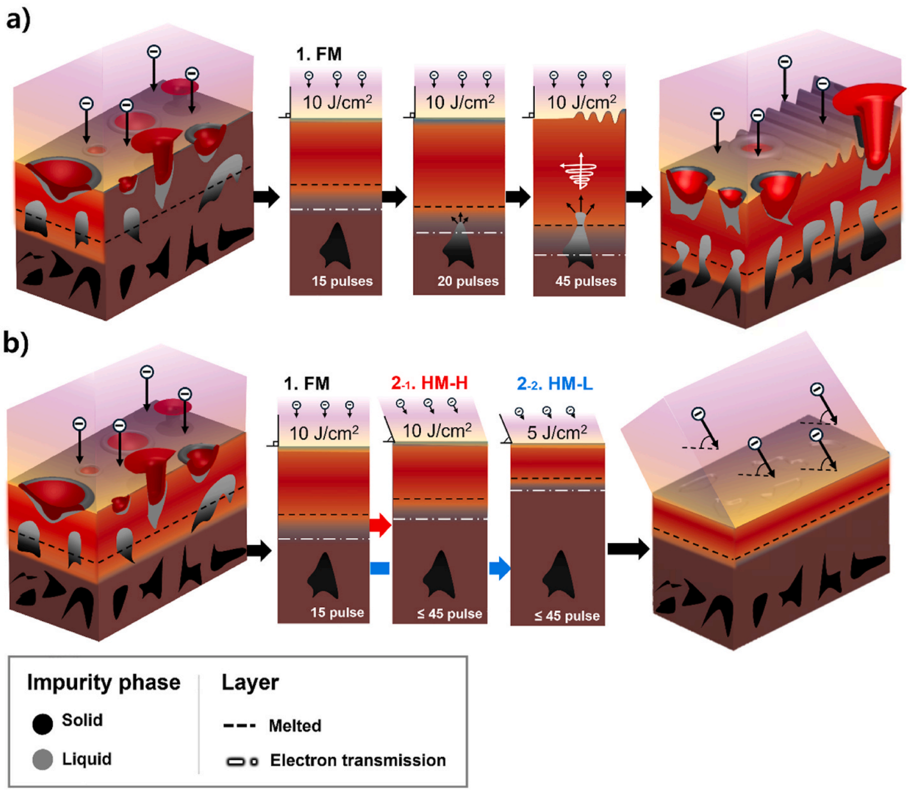

Fig. 8. Mechanisms of crater-like defect and wave pattern formation during LPEB treatment. a) FM condition: Increasing heat accumulation, deepening molten layer, intensifying surface defects. b) Comparison of FM, HM-H, HM-L: Control of molten layer depth, minimization of crater formation, and suppression of wave patterns in HM modes through angle adjustment and energy density reduction.

properties such as high hardness, corrosion resistance, and wear resistance [30,32]. Even if energy beam conditions are optimized to minimize crater-like defects, the overall effectiveness and reliability of the process could be significantly diminished if these critical surface properties are not maintained. Notably, surface hardness is a mechanical property closely associated with various surface characteristics such as fatigue resistance and wear resistance. As discussed in Section 4.1, FM 15, identified as the optimal process among the conditions with a standalone increase in pulse count (FM), achieved the highest Vickers hardness of 806 HV in Fig. 5a). However, as pulses were further added, the surface hardness dropped by up to 46.5%. This phenomenon is attributed to phase changes induced by LPEB, necessitating comprehensive metallurgical analyses, including XRD and microstructural observations.

For metallurgical analysis, an understanding of the phase diagram of H13 steel is essential. A phase diagram based on thermodynamic calculation for H13 steel was analyzed in a previous study, as shown in Fig. 9 [45,46]. Seven representative phases are identified between 600 °C and 2000 °C, and the temperatures corresponding to phase transformations are described as follows:

- Ae_{10}: Liquid (L) → L + delta ferrite (δ): Nucleation temperature of delta ferrite.
- Ae_9: L + δ → L + δ + austenite (γ): Nucleation temperature of austenite.
- Ae_8: L + δ + γ → L + γ: Transformation of delta ferrite into austenite.
- Ae_7: L + γ → γ: Melting point of H13 steel.
- Ae_6: γ → γ (+MC): Initial formation temperature of metallic carbide (MC).
- Ae_5: γ (+MC) → γ + alpha ferrite (α) (+MC): Transformation to alpha ferrite phase.
- Ae_3: γ + α (+MC) → α (+MC): Complete transformation to alpha ferrite.

Due to the high alloying element fraction of H13 steel, it is difficult to form diffusion-controlled structures such as bainite or pearlite. Instead, martensite, and carbides (MC, $M_{23}C_6$, etc.) are predominantly observed. In particular, for laser processing where a wide heat-affected zone is formed, detailed studies on the formation and distribution of carbides following hardness enhancement through laser surface treatment have already been conducted [33,34]. However, the LPEB process in this study is characterized by very rapid cooling rates, which limit or minimize the formation of carbides like MC. Therefore, MC carbide analysis is not a major focus of this study. Instead, the subsequent analyses concentrate on microstructural changes under non-equilibrium conditions and the resulting improvements in mechanical properties.

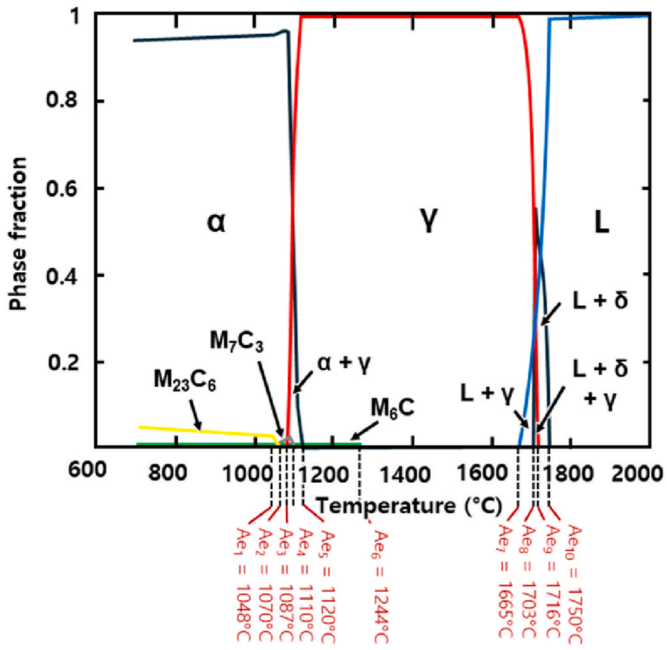

Fig. 9. Equilibrium phase diagram of AISI H13 steel elaborated by thermodynamic calculation [45,46].

While carbide formation is limited in LPEB treatment due to rapid cooling, this same cooling characteristic leads to unique phase transformation patterns. Due to the quenching stress caused by the rapid cooling gradient ($\sim 10^7$ K/sec) discussed in previous section, LPEB-treated surfaces are known to develop tensile residual stress, which can be confirmed by the XRD peak shifts before and after LPEB treatment shown in Fig. 7 [21,47]. The shift of the Bare peak toward larger angles (right direction) indicates decreased d-spacing, which represents tensile residual stress, confirming that tensile residual stress was induced in all treated conditions [21,48]. This quenching stress can also lead to different phase transformation patterns, which can be observed in the microstructure shown in Fig. 10. A notable feature in the etched microstructure shown in Fig. 10 is the differential etching rates observed among various phases. This characteristic enables phase identification through both morphological and chromatic analysis. Analysis was particularly focused on phases that exhibited excessive darkening due to rapid etching. Ferrite, exhibiting the highest corrosion and etching rate, typically presents a polyhedral morphology, and its accelerated etching rate is attributed to its inherent Body-Centered Cubic (BCC) soft phase structure. Conversely, surfaces that demonstrated high corrosion resistance after etching were identified as austenite phase and uniform martensite phase, known for their superior corrosion resistance. In FM 5 on Fig. 10a), clusters of black polyhedral phases surrounding yellow circular phases are observed in the surface morphology, which other studies have identified as delta ferrite encompassing martensite formed by quenching stress [20,30,49,50]. The existence of delta ferrite, a high-temperature phase, in LPEB treatment despite its extremely rapid cooling rate can be explained by the nucleation rate of austenite. When the cooling process passes through equilibrium transformation temperatures Ae_9 and Ae_8 in Fig. 9 very rapidly, limited austenite nucleation occurs, resulting in a surface structure with sparse austenite nuclei formation within ferrite [51,52]. During subsequent cooling, these austenite nuclei regions transform to martensite. In XRD analysis, this phase shows no difference from the Bare condition because both have BCC structures, making it crystallographically identical to alpha ferrite, however it is termed delta ferrite due to its unique formation process of remaining ferrite despite experiencing extremely rapid cooling of the molten layer.

The heat accumulation in the substrate with increasing pulse count was addressed in the 4.1. section. In terms of phase transformation, this thermal accumulation elevates the substrate temperature, consequently reducing the surface cooling rate. The decreased cooling rate allows for uniform distribution of austenite nuclei formation within the molten liquid across the surface, which subsequently transforms into complete martensite upon cooling. The broadening of ferrite peaks (211), (200), and (211) observed in the XRD patterns of FM 10 and FM 15 conditions, which exhibit the highest surface hardness levels among FM conditions, supports martensite formation, showing good correlation with hardness values. This microstructural evolution is further evidenced in the etched microstructures shown in Fig. 10. Fig. 10b) to 10c), representing FM 10 and FM 15 conditions respectively, clearly show needle-like martensite structures that remain distinguishable even after etching [49,50,53].

However, excessive heat accumulation and decreased cooling rates lead to the formation of alpha phase and increased retained austenite phase on the surface, resulting in reduced hardness. To prevent surface hardness reduction, it is effective to approach methods of increasing surface cooling rates through analysis of Fig. 2. The cooling rate is dependent on the temperature gradient between the surface and bulk, and larger temperature differences at the same depth result in steeper

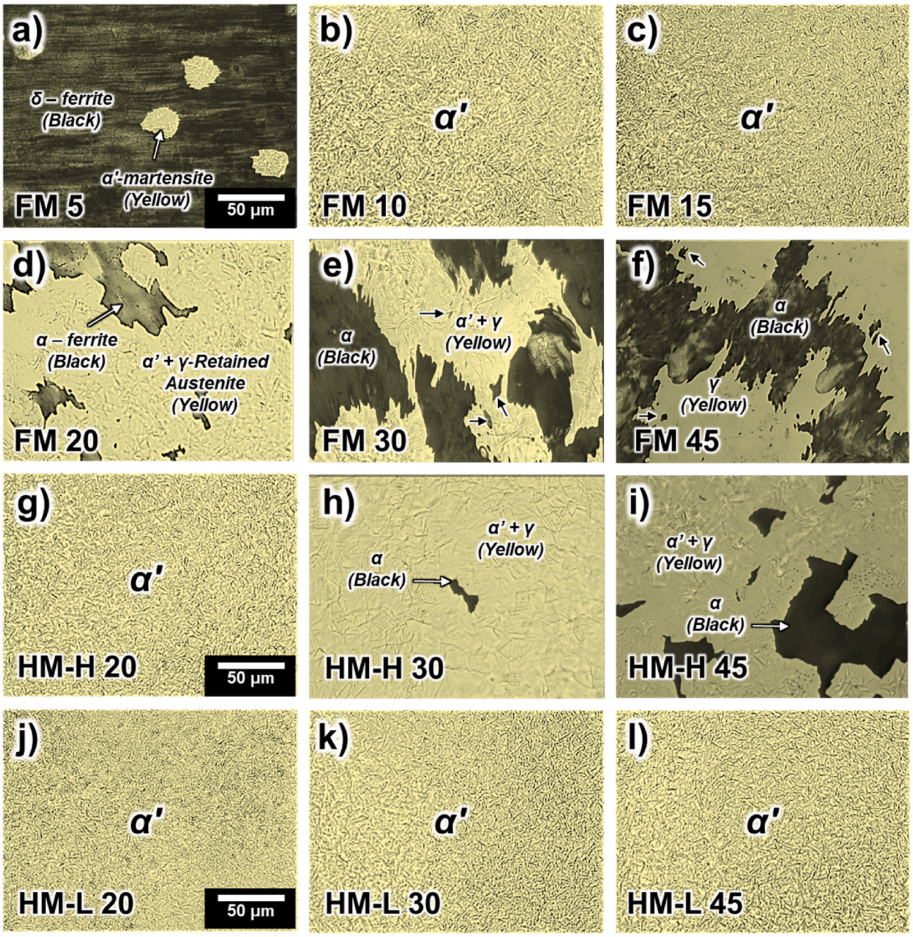

Fig. 10. Optical microscope (OM) images of chemically etched AISI H13 steel under different LPEB treatment conditions. Microstructural analysis under FM mode; a) to f) Microstructural analysis under HM-H mode; g) to i) Microstructural analysis under HM-L mode; j) to l).

temperature gradients at the surface, leading to faster cooling rates. Comparing the three conditions used in this study in Figs. 2–10 J/cm^2 at 0°, 10 J/cm^2 at 30°, and 5 J/cm^2 at 30° - shows that as the angle increases and energy density decreases, the graph's slope becomes steeper and maximum absorption increases. Notably, while the area under the 5 J/cm^2 graph is about half that of 10 J/cm^2, it shows a much higher peak point and steeper gradient. This analysis suggests that HM-H and HM-L conditions would have much faster cooling rates compared to conventional FM conditions.

These differences can be observed in the microstructure from Fig. 10. As pulse count increases from FM 20 onward, the area of polygonal alpha phases within the black regions increases, while the distribution of martensite needles decreases. The XRD data in Fig. 7a) also supports this, showing that the ferrite peaks that were broadened in FM 10 and 15 become sharp again, and the austenite peak becomes the main peak at the highest pulse count of FM 45. This indicates that the decreased cooling rate contributes to both increased retained austenite fraction and new formation of ferrite phases. However, excessive heat accumulation and decreased cooling rates lead to the formation of alpha phase and increased retained austenite phase on the surface, resulting in reduced hardness. To prevent surface hardness reduction, it is effective to approach methods of increasing surface cooling rates through analysis of Fig. 2. The cooling rate is dependent on the temperature gradient between the surface and bulk, and larger temperature differences at the same depth result in steeper temperature gradients at the surface, leading to faster cooling rates. Comparing the three conditions used in this study in Figs. 2–10 J/cm^2 at 0°, 10 J/cm^2 at 30°, and 5 J/cm^2 at 30° - shows that as the angle increases and energy density decreases, the graph's slope becomes steeper and maximum absorption increases. Notably, while the area under the 5 J/cm^2 graph is about half that of 10 J/cm^2, it shows a much higher peak point and steeper gradient. This analysis suggests that HM-H and HM-L conditions would have much faster cooling rates compared to conventional FM conditions. These differences can be observed in the microstructure on Fig. 10. As pulse count increases from FM 20 onward, the area of polygonal alpha phases within the black regions increases, while the distribution of martensite needles decreases. Interestingly, unlike the polygonal aggregate morphology of alpha phase in HM-H, the alpha phase and retained austenite in FM 30 and FM 45 exhibit blade-like elongated patterns with distinct directional alignment. This directional structure is formed by shockwaves generated from the explosion of localized melt pools beneath the molten layer due to heat accumulation, which influences the orientation of austenite nuclei in the liquid phase. As a result of directional solidification induced by these shockwaves, the alpha ferrite formed from these aligned austenite islands inherits this elongated directional morphology. The small black phases observed on the austenite islands (black arrow) in FM 30 and FM 45 conditions of Fig. 10 are analyzed to be alpha ferrite, which formed through the decomposition of martensite into alpha phase and carbides due to heat accumulation effects [33,34]. The XRD data in Fig. 7a) also shows that the ferrite peaks that were broadened in FM 10 and 15 become sharp again, and the fact that the austenite peak with (111) lattice structure becomes the main peak at the highest pulse count of FM 45 indicates that the decreased cooling rate contributes to both increased retained austenite fraction and new formation of ferrite phases.

HM-H was analyzed to have a higher cooling rate than FM. Unlike

FM 20 where alpha ferrite phase could be observed, HM-H 20 showed complete martensite formation on the surface, with alpha phase beginning to form and gradually expanding from HM-H 30 onward. The generated alpha ferrite shows a more polygonal morphology compared to FM 30 and FM 45, indicating minimal influence from subsurface explosions caused by heat accumulation of a substrate under the molten layer. In the XRD graph of Fig. 7b), HM-H 20 showed similar ferrite peak broadening to FM 10 and FM 15 in Figure a), and these peaks became sharp again after HM-H 30. HM-H also shows an increasing trend in the (111) austenite lattice structure. The (111) plane, being the most stable lattice structure, generally requires relatively lower energy, and the heat accumulation seems to have facilitated its preferential growth [54,55]. This suggests that both FM and HM-H are affected by heat accumulation, resulting in decreased cooling rates. The hardness analysis in Fig. 5 also shows that FM and HM-H exhibit similar trends of decreasing hardness as pulse count increases, although to different degrees. However, unlike the FM condition, the HM-H condition shows dominance of the (220) austenite peak. The (220) plane, which generally requires higher energy than the (111) plane, benefitted from the surface energy concentration induced by the angle, facilitating its growth [56,57]. This observation is consistent across the HM-L condition as well, where the (220) plane exhibited greater prominence compared to the (111) plane in all HM conditions. Unlike FM and HM-H, HM-L maintained complete martensite phase even at maximum pulse count (Fig. 10j) to 10l)), and its hardness remained consistent within 4% of maximum hardness, indicating minimal decrease in cooling rate. This is supported by the peak separation phenomenon beyond (200) ferrite peak broadening, decreased (111) austenite peak fraction, and uniform XRD graphs showing no variability despite increased pulses (Fig. 6c)). Interestingly, compared to the rise in (220) austenite lattice structure peak in HM-H, the HM-L condition showed simultaneous increases in both (220) and (200) peaks. The (200) plane, possessing square symmetry and a simpler arrangement compared to the (220) plane, can preferentially form under rapid cooling conditions. Through this analysis, it was concluded that the prominent increase in (220) and (200) austenite peaks in HM-L was due to it having the highest surface energy concentration and fastest cooling rate.

A continuous cooling transformation (CCT) diagram incorporating cooling rate information can be constructed by integrating all experimental results and analyses. The CCT diagram of H13 steel (Fig. 11) serves as a reference material showing qualitative trends in phase transformation behavior, and since its purpose is to help understand general transformation tendencies rather than provide exact numerical values, experimental verification is necessary for actual process design. Most iron-based CCT diagrams share similar basic structures, with main differences being the x-axis position of phase node points, y-axis phase transformation temperatures, and the formation of new phases. This diagram's node points for the gray graphs were constructed by referencing CCT diagrams of similarly composed 9Cr–1Mo steel and H13 steel's time-temperature transformation (TTT) diagram [51,56], while the y-axis was modified based on the phase transformation temperatures (from Ae_{10} to Ae_1) from the H13 steel equilibrium phase diagram in Fig. 9. Notably, for alloy steels like H13, the CCT diagram was constructed to reflect the position of metallic carbides, which do not form in ordinary carbon steels.

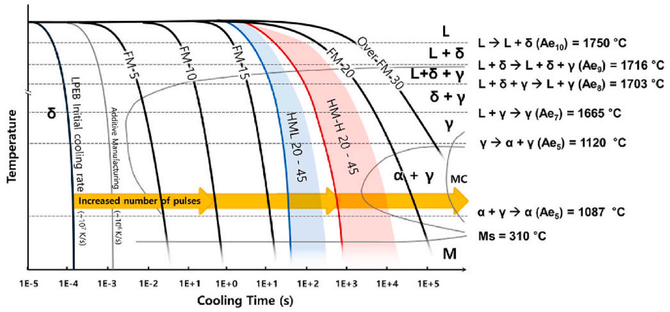

Fig. 11. CCT diagram illustrating heat accumulation and phase transformation for FM (black), HM-H (red), and HM-L (blue) cooling conditions.

For the single LPEB pulse case, the theoretical cooling rate is 10^7 K/s, which is faster than the theoretical value of 10^6 K/s for laser-based additive manufacturing, placing it at the leftmost position on the graph. In this case, the speed passing through the austenite nucleation region ($Ae_7 < T < Ae_9$) is very fast, forming delta ferrite. For FM 5, it passes slightly through the austenite nucleation region shown in gray lines, transforming the formed austenite into martensite, while FM 10 and FM 15 ensure sufficient area through the austenite phase, forming a high fraction of martensite. From FM 20, the slope becomes gentler and passes through the alpha phase formation graph, indicating decreased cooling rate and formation of new alpha ferrite. As the slope increases thereafter, the proportion of austenite and alpha ferrite phases increases (FM 45). For the HM condition, which showed high degree of surface absorption and steep temperature gradient, the austenite phase fraction commonly increases significantly, resulting in a gentle speed through $Ae_7 < T < Ae_9$ followed by steep graphs. The diagram progresses from FM 15 to HM-L with less heat accumulation, and then to HM-H, where HM-L with consistent surface microstructure and properties shows a narrow range, while HM-H displays a wider range due to additional pulse numbers and heat accumulation leading to alpha phase formation.

4.3. *Optimizations and recommendations*

The optimization of LPEB treatment parameters requires a comprehensive analysis considering both surface defect prevention and mechanical property enhancement. From the surface defect perspective, the HM-L condition demonstrated superior results with the lowest crater density ($0.55 \times 10^7/m^2$) and surface roughness (0.2 $\mu m R_a$). This significant improvement over conventional FM conditions can be attributed to the combined effects of increased incidence angle (30°) and reduced energy density (5 J/cm^2), which effectively controlled the depth-dependent absorption and prevented excessive heat accumulation. In terms of microstructure and hardness optimization, the results revealed distinct patterns across different treatment conditions. The FM mode showed optimal hardness (840 HV) at FM 15, however it experienced significant degradation with additional pulses due to heat accumulation effects. The HM-H condition maintained relatively higher hardness levels compared to FM but still showed some decrease at higher pulse counts. Notably, the HM-L condition demonstrated the most stable performance, maintaining consistent hardness values (within 4% variation from maximum) even at high pulse counts, while preserving a uniform martensitic structure throughout the treatment process. When considering all parameters comprehensively, the HM-L condition with 30 pulses emerges as the optimal treatment parameter set, achieving minimal surface defects, excellent surface smoothness, stable high hardness, and uniform martensitic microstructure with minimal heat accumulation effects. Previous studies have shown that surface properties achieved through LPEB treatment can significantly affect corrosion resistance through microstructural characteristics. For example, FCC austenite structure shows superior corrosion resistance compared to BCC ferrite structure, and the formation of uniform martensitic structures can enhance overall corrosion resistance [50,53,55]. Furthermore, research has demonstrated that corrosion typically initiates at non-metallic inclusions exposed in crater defects [30,57]. The significant reduction in crater defects and controlled phase transformation achieved under HM-L conditions therefore suggests potential improvements in corrosion resistance by eliminating vulnerable sites and maintaining beneficial microstructural characteristics. The stable microstructure and minimal surface defects achieved under HM-L conditions thus provide an excellent foundation for investigating enhanced corrosion resistance in industrial applications, particularly in high-value-added industries such as semiconductor manufacturing and precision molding. This optimization approach, focusing on depth-dependent absorption control, could be extended to other metallic materials and different industrial applications where surface quality and mechanical properties are critical factors.

5. Conclusions

This study successfully developed optimized Large Pulsed Electron Beam (LPEB) irradiation conditions for surface treatment of AISI H13 steel, focusing on minimizing crater-like surface defects while maintaining excellent surface properties. The conventional approach of increasing pulse counts showed limitations in removing non-metallic inclusions and led to excessive heat accumulation, resulting in increased melt layer depth and introduction of new non-metallic inclusions. These issues have constrained industrial applications due to degradation of surface properties.

To address these challenges, this study proposed a novel approach controlling the depth-dependent energy absorption of LPEB. Unlike previous studies that focused solely on optimizing process parameters, this research systematically analyzed the relationship between irradiation angle and energy density, achieving process design based on energy absorption mechanisms. The developed hybrid mode (HM) conditions successfully controlled heat accumulation while improving surface quality. Particularly, the HM-L condition, combining increased irradiation angle and reduced energy density, demonstrated significantly lower defect density and superior surface properties compared to conventional methods. This was achieved without complex process steps or additional equipment, enhancing process economics and practicality. Furthermore, stable results across process condition variations proved the reliability and reproducibility of this method.

In conclusion, the depth-dependent energy absorption control method developed in this study presents new possibilities for electron beam surface treatment technology. This approach can be extended to various metallic materials and applied to developing automated optimization systems for process parameters. Further research is expected in scale-up studies for large-area treatment and practical applications in high-precision industries such as mold finishing and semiconductor manufacturing. The results of this study are expected to contribute to expanding the industrial applications of electron beam surface treatment technology.

Declaration of competing interest

The authors declare that they have no known competing financial interests or personal relationships that could have appeared to influence the work reported in this paper.

Acknowledgments

This work was supported by the National Research Foundation of Korea (NRF) funded by the Ministry of Education (2021R1I1A3045191), and the Ministry of Science and ICT of Korea (2022R1A2C3007963, RS-2024-00348205).

Appendix A. Supplementary data

Supplementary data to this article can be found online at https://doi.org/10.1016/j.jmrt.2024.11.254.

References

[1] Molaei M, Fattah-alhosseini A, Nouri M, Kaseem M. Assessing the wear properties of plasma electrolytic oxidation TiO2 coatings incorporated ZrO2 nanoparticles on Cp-Ti in simulated body fluid. Appl Surf Sci Adv 2024;19:100563. https://doi.org/10.1016/j.apsadv.2023.100563.

[2] Zhao Y, Mei H, Chang P, Yang Y, Cheng L, Zhang L. Biomimicking synovial joints trans-scale structured AgQDs/MXene/SiOC achieving macroscale high lubrication and superior wear resistance. J Mater Sci Technol 2024;174:63–73. https://doi.org/10.1016/j.jmst.2023.07.030.

[3] Wang B, Lei J, Han H, Wang T, Jia X, Lei J. Inconel 718 alloy reinforced with nano-sized WC particles and graphene nanoplatelets: microstructure, wear resistance and electrochemical properties. J Alloys Compd 2024;1002:175070. https://doi.org/10.1016/j.jallcom.2024.175070.

[4] Hu Y, Wang H, Wang D, Xia X, Liu N, Yang T, et al. In situ preparation of nano cone-like structures on 3D printed titanium alloy implants via one-step femtosecond laser manufacturing for better osseointegration, anti-corrosion, and anti-fatigue. J Mater Sci Technol 2025;206:88–99. https://doi.org/10.1016/j.jmst.2024.03.070.

[5] Zhu X, Ding J, Mo Z, Jiang X, Sun J, Fu H, et al. Evaluation of chemical mechanical polishing characteristics using mixed abrasive slurry: a study on polishing behavior and material removal mechanism. Appl Surf Sci 2025;679:161157. https://doi.org/10.1016/j.apsusc.2024.161157.

[6] Deng T, Li J, Zheng Z. Fundamental aspects and recent developments in metal surface polishing with energy beam irradiation. Int J Mach Tool Manufact 2020;148:103472. https://doi.org/10.1016/j.ijmachtools.2019.103472.

[7] Datta D, Rai H, Singh S, Srivastava M, Sharma RK, Gosvami NN. Nanoscale tribological aspects of chemical mechanical polishing: a review. Appl Surf Sci Adv 2022;11:100286. https://doi.org/10.1016/j.apsadv.2022.100286.

[8] Zhu W-L, Beaucamp A. Compliant grinding and polishing: a review. Int J Mach Tool Manufact 2020;158:103634. https://doi.org/10.1016/j.ijmachtools.2020.103634.

[9] Tsai MJ, Chang J-L, Haung J-F. Development of an automatic mold polishing system. IEEE Trans Autom Sci Eng 2005;2:393–7. https://doi.org/10.1109/TASE.2005.853723.

[10] Deng X, Ma Y, Zhang P, Zhang W, Chen S, Xiao S, et al. Investigation of shadow effect in laser-focused atomic deposition. Appl Surf Sci 2012;261:464–9. https://doi.org/10.1016/j.apsusc.2012.08.033.

[11] Kim J, Lee WJ, Park HW. Temperature predictive model of the large pulsed electron beam (LPEB) irradiation on engineering alloys. Appl Therm Eng 2018;128:151–8. https://doi.org/10.1016/j.applthermaleng.2017.08.142.

[12] Negi S, Nambolan AA, Kapil S, Joshi PS, R M, Karunakaran KP, et al. Review on electron beam based additive manufacturing. Rapid Prototyp J 2020;26:485–98. https://doi.org/10.1108/RPJ-07-2019-0182.

[13] Jain VK, Choudhury SK, Ramesh KM. On the machining of alumina and glass. Int J Mach Tool Manufact 2002;42:1269–76. https://doi.org/10.1016/S0032-3861(02)00241-0.

[14] Proskurovsky DI, Rotshtein VP, Ozur GE, Markov AB, Nazarov DS, Shulov VA, et al. Pulsed electron-beam technology for surface modification of metallic materials. J Vac Sci Technol A 1998;16:2480–8. https://doi.org/10.1116/1.581369.

[15] Perry AJ, Matossian JN, Vajo JJ, Doty RE, Bull SJ, Page TF, et al. Rapid thermal processing of TiN coatings deposited by chemical and physical vapor deposition using a low-energy, high-current electron beam: microstructural studies and properties. Metall Mater Trans A 1999;30:2931–9. https://doi.org/10.1007/s11661-999-0130-9.

[16] Deka BK, Kong K, Park Y-B, Park HW. Large pulsed electron beam (LPEB)-processed woven carbon fiber/ZnO nanorod/polyester resin composites. Compos Sci Technol 2014;102:106–12. https://doi.org/10.1016/j.compscitech.2014.07.026.

[17] Uno Y, Okada A, Uemura K, Raharjo P, Furukawa T, Karato K. High-efficiency finishing process for metal mold by large-area electron beam irradiation. Precis Eng 2005;29:449–55. https://doi.org/10.1016/j.precisioneng.2004.12.005.

[18] Pogrebnjak AD, Bratushka S, Boyko VI, Shamanin IV, Tsvintarnaya YuV. A review of mixing processes in Ta/Fe and Mo/Fe systems treated by high current electron beams. Nucl Instrum Methods Phys Res Sect B Beam Interact Mater Atoms 1998;145:373–90. https://doi.org/10.1016/S0168-583X(98)00417-0.

[19] Feng Z, Wang J, Zhang F, Liu J, Hu J, Chai L, et al. Effect of high current pulsed electron beam on surface microstructure and properties of cold-rolled austenitic stainless steel. J Mater Res Technol 2024;29:1183–93. https://doi.org/10.1016/j.jmrt.2024.01.103.

[20] Qin Y, Zou J, Dong C, Wang X, Wu A, Liu Y, et al. Temperature–stress fields and related phenomena induced by a high current pulsed electron beam. Nucl Instrum Methods Phys Res Sect B Beam Interact Mater Atoms 2004;225:544–54. https://doi.org/10.1016/j.nimb.2004.06.008.

[21] Lee Y, Choe J-H, Jang Y-J, Kim J, Yim C, Kim J. A delamination prevention of tetrahedral amorphous carbon (ta-C) coating using large pulsed electron beam (LPEB) pretreatment. Surf Coating Technol 2022;440:128485. https://doi.org/10.1016/j.surfcoat.2022.128485.

[22] Lee WJ, Kim J, Park HW. Improved corrosion resistance of Mg alloy AZ31B induced by selective evaporation of Mg using large pulsed electron beam irradiation. J Mater Sci Technol 2019;35:891–901. https://doi.org/10.1016/j.jmst.2018.12.004.

[23] Zhang K, Zou J, Grosdidier T, Dong C. Formation and evolution of craters in carbon steels during low-energy high-current pulsed electron-beam treatment. J Vac Sci Technol A: Vacuum, Surf., Films 2009;27:1217–26. https://doi.org/10.1116/1.3207948.

[24] Gao Y, Qin Y, Dong C, Li G. From crater eruption to surface purification of raw silicon: a treatment by pulsed electron beam. Appl Surf Sci 2014;311:413–21. https://doi.org/10.1016/j.apsusc.2014.05.076.

[25] Cai J, Guan Q, Lv P, Zhang C, Yin Y. Crater formation on the surface of pure metal and alloy irradiated by high current pulsed electron beam. High Temp Mater Process 2018;37:777–84. https://doi.org/10.1515/htmp-2017-0067.

[26] Qin Y, Dong C, Wang X, Hao S, Wu A, Zou J, et al. Temperature profile and crater formation induced in high-current pulsed electron beam processing. J Vac Sci Technol A 2003;21:1934–8. https://doi.org/10.1116/1.1619417.

[27] Zou J, Zhang K, Dong C, Qin Y, Hao S, Grosdidier T. Selective surface purification via crater eruption under pulsed electron beam irradiation. Appl Phys Lett 2006; 89:041913. https://doi.org/10.1063/1.2234306.

[28] Wu B, Tang G, Zhao X, Wang L, Gu L. Texturing effect of cratercrater-like cavities induced by high-current pulsed electron beam (HCPEB) irradiation. Coatings 2018; 8:355. https://doi.org/10.3390/coatings8100355.

[29] Yu Z, Wang ZG, Yamazaki K, Sano S. Surface finishing of die and tool steels via plasma-based electron beam irradiation. J Mater Process Technol 2006;180: 246–52. https://doi.org/10.1016/j.jmatprotec.2006.06.014.

[30] Zou JX, Zhang KM, Hao SZ, Dong C, Grosdidier T. Mechanisms of hardening, wear and corrosion improvement of 316 L stainless steel by low energy high current pulsed electron beam surface treatment. Thin Solid Films 2010;519:1404–15. https://doi.org/10.1016/j.tsf.2010.09.022.

[31] Hwang Y, Kim J, Yim C, Park HW. Deep-sintered copper tracks for thermal oxidation resistance using large pulsed electron beam. ACS Omega 2021;6: 19134–43. https://doi.org/10.1021/acsomega.1c02475.

[32] Sankara Narayanan TSN, Kim J, Park HW. High performance corrosion and wear resistant Ti-6Al-4V alloy by the hybrid treatment method. Appl Surf Sci 2020;504: 144388. https://doi.org/10.1016/j.apsusc.2019.144388.

[33] Telasang G, Dutta Majumdar J, Wasekar N, Padmanabham G, Manna I. Microstructure and mechanical properties of laser clad and post-cladding tempered AISI H13 tool steel. Metall Mater Trans A 2015;46:2309–21. https://doi.org/10.1007/s11661-015-2757-z.

[34] Telasang G, Dutta Majumdar J, Padmanabham G, Manna I. Structure–property correlation in laser surface treated AISI H13 tool steel for improved mechanical properties. Mater Sci Eng, A 2014;599:255–67. https://doi.org/10.1016/j.msea.2014.01.083.

[35] Markov AB, Rotshtein VP. The mechanism of increase of the thickness of the zone of thermal effect during pulse-periodic treatment of a target by an electron beam. High Temp 2000;38:15–9. https://doi.org/10.1007/BF02755560.

[36] Markov A, Solovyov A, Yakovlev E, Slobodyan M. Prediction of the composition of surface alloys formed via pulsed melting of preliminary deposited coatings. Mater Chem Phys 2022;292:126821. https://doi.org/10.1016/j.matchemphys.2022.126821.

[37] Reimer L. Emission of backscattered and secondary electrons. In: Reimer L, editor. Scanning electron microscopy: physics of image formation and microanalysis. Berlin, Heidelberg: Springer; 1998. p. 135–69. https://doi.org/10.1007/978-3-540-38967-5_4.

[38] Niedrig H. Electron backscattering from thin films. J Appl Phys 1982;53:R15–49. https://doi.org/10.1063/1.331005.

[39] Cosslett VE, Thomas RN. Multiple scattering of 5-30 keV electrons in evaporated metal films: I. Total transmission and angular distribution. Br J Appl Phys 1964;15: 883. https://doi.org/10.1088/0508-3443/15/8/303.

[40] Cosslett VE, Thomas RN. Multiple scattering of 5-30 keV electrons in evaporated metal films II: range-energy relations. Br J Appl Phys 1964;15:1283. https://doi.org/10.1088/0508-3443/15/11/305.

[41] Cosslett VE, Thomas RN. Multiple scattering of 5 - 30 keV electrons in evaporated metal films III: backscattering and absorption. Br J Appl Phys 1965;16:779. https://doi.org/10.1088/0508-3443/16/6/303.

[42] Kanaya K, Ono S. The energy dependence of a diffusion model of an electron probe into solid targets. J Phys D Appl Phys 1978;11:1495. https://doi.org/10.1088/0022-3727/11/11/008.

[43] Neubert G, Rogaschewski S. In: Görlich, editor. Backscattering coefficient measurements of 15 to 60 keV electrons for solids at various angles of incidence. De Gruyter; 2022. p. 35–42. https://doi.org/10.1515/9783112501726-005. 59, Number 1 May 16.

[44] Staub P-F. Bulk target backscattering coefficient and energy distribution of 0.5-100 keV electrons: an empirical and synthetic study. J Phys D Appl Phys 1994;27:1533. https://doi.org/10.1088/0022-3727/27/7/030.

[45] Wu L, Das S, Gridin W, Leuders S, Kahlert M, Vollmer M, et al. Hot work tool steel processed by laser powder bed fusion: a review on most relevant influencing factors. Adv Eng Mater 2021;23:2100049. https://doi.org/10.1002/adem.202100049.

[46] Yan J, Song H, Dong Y, Quach W-M, Yan M. High strength (~2000 MPa) or highly ductile (~11%) additively manufactured H13 by tempering at different conditions. Mater Sci Eng, A 2020;773:138845. https://doi.org/10.1016/j.msea.2019.138845.

[47] Zhang KM, Zou JX, Bolle B, Grosdidier T. Evolution of residual stress states in surface layers of an AISI D2 steel treated by low energy high current pulsed electron beam. Vacuum 2013;87:60–8. https://doi.org/10.1016/j.vacuum.2012.03.061.

[48] Choe J-H, Park S, Choe J-S, Kim DM, Kim J. Effect of a large pulsed electron beam (LPEB) irradiation on mechanical properties and fatigue behavior of Ti-6Al-4V. J Mech Sci Technol 2022;36:2913–22. https://doi.org/10.1007/s12206-022-0523-x.

[49] Hao S, Wu P, Zou J, Grosdidier T, Dong C. Microstructure evolution occurring in the modified surface of 316L stainless steel under high current pulsed electron beam treatment. Appl Surf Sci 2007;253:5349–54. https://doi.org/10.1016/j.apsusc.2006.12.011.

[50] Zou J, Grosdidier T, Zhang K, Dong C. Mechanisms of nanostructure and metastable phase formations in the surface melted layers of a HCPEB-treated D2 steel. Acta Mater 2006;54:5409–19. https://doi.org/10.1016/j.actamat.2006.05.053.

[51] Villaret F, Boulnat X, Aubry P, Zollinger J, Fabrègue D, de Carlan Y. Modelling of delta ferrite to austenite phase transformation kinetics in martensitic steels: application to rapid cooling in additive manufacturing. Materialia 2021;18: 101157. https://doi.org/10.1016/j.mtla.2021.101157.

[52] Li X, Gao F, Jiao J, Cao G, Wang Y, Liu Z. Influences of cooling rates on delta ferrite of nuclear power 316H austenitic stainless steel. Mater Char 2021;174:111029. https://doi.org/10.1016/j.matchar.2021.111029.

[53] Samih Y, Marcos G, Stein N, Allain N, Fleury E, Dong C, et al. Microstructure modifications and associated hardness and corrosion improvements in the AISI 420 martensitic stainless steel treated by high current pulsed electron beam (HCPEB). Surf Coating Technol 2014;259:737–45. https://doi.org/10.1016/j.surfcoat.2014.09.065.

[54] Brunatto SF, Cardoso RP, Santos LL. Behavior of retained austenite and carbide phases in AISI 440C martensitic stainless steel under cavitation. Eng 2024;5: 1980–94. https://doi.org/10.3390/eng5030105.

[55] Porter DA, Easterling KE, Sherif MYA. Phase transformations in metals and alloys. third ed. Boca Raton, FL: CRC Press; 2009.

[56] Is TTT diagram of tool steel H13 useful ? -. Is TTT diagram of tool steel H13 useful. https://www.viratsteel.in/blog/is-ttt-diagram-of-tool-steel-h13-useful/. [Accessed 24 November 2024].

[57] Kim J, Park SS, Park HW. Corrosion inhibition and surface hardening of KP1 and KP4 mold steels using pulsed electron beam treatment. Corrosion Sci 2014;89: 179–88. https://doi.org/10.1016/j.corsci.2014.08.018.